

A combination method to generate fluctuating boundary conditions for large eddy simulation

Dayang Wang^{*1}, X.J. Yu², Y. Zhou¹ and K.T. Tse²

¹School of Civil Engineering, Guangzhou University, Guangzhou 510006, P.R. China

²Department of Civil and Environmental Engineering, Hong Kong University of Science and Technology, Clear Water Bay, Kowloon, Hong Kong

(Received July 16, 2014, Revised February 18, 2015, Accepted March 6, 2015)

Abstract. A Combination Random Flow Generation (CRFG) technique for obtaining the fluctuating inflow boundary conditions for Large Eddy Simulation (LES) is proposed. The CRFG technique was developed by combining the typical RFG technique with a novel calculation of k and ε to estimate the length- and time-scales (l , τ) of the target fluctuating turbulence field used as the inflow boundary conditions. Through comparatively analyzing the CRFG technique and other existing numerical/experimental results, the CRFG technique was verified for the generation of turbulent wind velocity fields with prescribed turbulent statistics. Using the turbulent velocity fluctuations generated by the CRFG technique, a series of LESs were conducted to investigate the wind flow around S-, R-, L- and U-shaped building models. As the pressures of the models were also measured in wind tunnel tests, the validity of the LES, and the effectiveness of the inflow boundary generated by the CRFG techniques were evaluated through comparing the simulation results to the wind tunnel measurements. The comparison showed that the LES accurately and reliably simulates the wind-induced pressure distributions on the building surfaces, which indirectly validates the CRFG technique in generating realistic fluctuating wind velocities for use in the LES. In addition to the pressure distribution, the LES results were investigated in terms of wind velocity profiles around the building models to reveal the wind flow dynamics around bluff bodies. The LES results quantitatively showed the decay of the bluff body influence when the flow moves away from the building model.

Keywords: computational wind engineering; large eddy simulation; inflow boundary condition; random turbulence generation technique; wind pressure characteristic; wind velocity profile

1. Introduction

The use of Large Eddy Simulation (LES) to simulate turbulent flow fields in computational fluid dynamics has continuously increased, keeping pace with the growth of the available computational power. The large number of computation cells in a grid discrete system, which is required to simulate flows with high Reynolds number in the LES framework, can be accomplished with super-computers or even regular workstations with high-profile hardware. In addition, a series of improvements in LES with respect to the sub-grid scale model, sub-grid

*Corresponding author, Professor, E-mail: wadaya2006@aliyun.com

scale filtering, numerical schemes and extensions to the unstructured grid system, have made LES very appealing in solving engineering flow dynamic problems (Tunay *et al.* 2013, Dagneu and Bitsuamlak 2014). One problem hindering LES development, generating turbulent inflows with realistic statistical characteristics, has not yet been conclusively solved and needs further investigation. Due to its importance, a considerable amount of research has been conducted to provide a way to generate fluctuating wind velocities for use as inflow boundary conditions for LES, (Hoshiya 1972, Kondo *et al.* 1997, Tamura 2000, Batten *et al.* 2004).

When applying the LES technique to simulate wind flows around buildings, it is important to reconstruct the three-dimensional turbulent fluctuating wind field, whose statistical characteristics follow the prescribed values, to be used as the inflow boundary conditions. There are several methods to generate the turbulent fluctuating wind field for use as the inflow turbulence boundary conditions and they can be classified into four categories (Keating *et al.* 2004). The first category uses inflow data from a precursor simulation to model the turbulent inflow, which requires a precursor simulation is completed before the actual simulation in the domain of interest (Churchfield *et al.* 2012, Richard *et al.* 2014).

The second category adopts the power spectral density and cross-spectral density obtained from Fast Fourier Transformation (FFT) analyses in order to construct trigonometric series with Gaussian random coefficients and the velocity fluctuations are then expressed as the sum of a series of trigonometric fluctuations (Hoshiya 1972). The third category uses a random 2D vortex method to add perturbations, whose magnitudes are determined by the required statistics, onto a specified mean velocity profile (Mathey *et al.* 2006). The last category is based on a variant of the spectral method which generates an isotropic and continuous flow field (Kraichnan 1970). There are some limitations regarding the turbulent fluctuating wind field generated by the methods belonging to the first second and third categories (Huang *et al.* 2010). In particular, the fluctuating wind field generated by the first category method may violate the continuity constraint as the divergence-free constraint is imposed in the generation process. The target spectrum and other statistical characteristics of the generated fluctuating wind field are also not explicitly expressed when using the methods in the second category. Hence, we focus on the third category in this study.

Kraichnan (1970) investigated the single-particle diffusion process in a multivariate-normal, incompressible, stationary, isotropic wind velocity field in three dimensions by the numerical simulation approach and proposed firstly a method of generating an isotropic continuous flow field based on a variant of spectral method. The turbulence length scale and time scale are incorporated into the basic model by Kraichnan so as to generate an isotropic divergence-free fluctuating velocity field with the target turbulence length and time scales. The results showed that the simulated fluctuating velocity field agrees with Taylor's picture of a classical diffusion process when the time scale is comparable with the eddy circulation time. Kondo *et al.* (1997) modified this generation method using a Monte Carlo simulation approach in order to make the target power spectral density and cross-spectral density satisfy the continuity constraint. As a result, the level of the velocity divergence in the generated fluctuating velocity field is greatly reduced. Klein (2003) proposed a method to generate an artificial fluctuating velocity field based on applying a digital-filtering process to the pseudo random data, yielding a pseudo random field with prescribed second-order statistics. Keating *et al.* (2004) simulated boundary-layer flows using two synthetic inflow boundary conditions: (a) inflow fluctuating velocities generated based on the synthetic turbulence generation method of Batten *et al.* (2004), and (b) inflow fluctuating velocities generated based on the same method with controlled forces applied at discrete planes downstream

of the inflow boundary. The results showed that the computational overhead of these turbulent inflow generations is small and they are adaptable to simulate non-equilibrium flows. Smirnov *et al.* (2001) presented a random flow generation (RFG) technique, based on synthesizing divergence-free vector fields from a sample of Fourier harmonics. The RFG technique allows the generation of a non-homogeneous anisotropic flow field showing the turbulent velocity fluctuations. The non-homogeneous, anisotropic turbulent flow generated using the RFG technique can be used as initial/inlet boundary conditions in the LES. In addition, the RFG technique, in combination with the LES, is suitable for simulating high-Reynolds number flows. Recently, Huang *et al.* (2010) presented a general inflow turbulence generator based on the Discretizing and Synthesizing Random Flow Generation (DSRFG) technique, which is capable of generating a turbulent flow field with the spectral characteristics agreeing with any given values. In their study, a parameter analysis was presented on the turbulence integral length scales models, (a) turbulence scale $l = (C_\mu)^{0.75} k^{1.5} / \varepsilon$ as in Smirnov *et al.* (2001) where k is the turbulence kinetic energy, ε is the dissipation rate and $C_\mu = 0.09$, (b) a constant length scale L ($L_u = L_v = L_w = L = 0.3$ m, where L_u, L_v, L_w are the turbulence integral length scales in three spatial directions), and (c) the reduced length scale $C_L L$ (where C_L is a constant between 1 and 2). From parametric analysis, it has been found that “it is clear that the spatial correlation generated by the RFG is erroneous in the shape of the correlation curve as compared with the target and that generated by the DSRFG”. The numerical results of Li *et al.* (2010) showed that a spatially correlated turbulent flow field, which is used as the inflow boundary condition for the LES, could be generated by the approach suggested by Huang *et al.* (2010).

The aim of this study is to establish an inflow condition generation method for the LES which is capable of obtaining a spatially correlated turbulent flow field satisfying the prescribed power spectra, such as the von Karman spectrum (Lumley and Panofsky 1964, Hinze 1975). Using the established inflow boundary condition generation method, wind flows around four irregular shaped bluff bodies are then simulated based on LES techniques. Wind tunnel test results and theoretical calculations are then utilized to validate the LES outputs. In addition, the characteristics of the mean and the fluctuating pressure coefficient distributions and the vertical and lateral velocity profiles around bluff bodies have been investigated and are discussed in detail.

2. Review of RFG technique

Based on the Kraichnan’s spectral method (Kraichnan 1970) for the generation of an isotropic continuous flow field, Smirnov *et al.* (2001) presented an RFG technique to generate an anisotropic flow field, which involves a scaling and orthogonal transformation process applied to a continuous flow field generated through summing a series of harmonic functions. Given an anisotropic velocity correlation tensor (Smirnov *et al.* 2001)

$$r_{ij} = \overline{\tilde{u}_i \tilde{u}_j} \tag{1}$$

of a turbulent flow field $\{\tilde{u}_i(x_j, t)\}_{i,j=1,2,3}$, find an orthogonal transformation tensor a_{ij} that would diagonalize r_{ij}

$$\begin{cases} a_{mi} a_{nj} r_{ij} = \delta_{mn} c_{(n)}^2 \\ a_{ik} a_{kj} = \delta_{ij} \end{cases} \tag{2}$$

As a result, both a_{ij} and c_n become known functions of space. In the new coordinate system defined by the transformation tensor a_{ij} , the coefficients $c_n = \{c_1, c_2, c_3\}$ correspond to the turbulent fluctuating velocities (u', v', w') in the conventional spatial coordinate system.

A transient velocity field $\{v_i(x_j, t)\}_{i,j=1,2,3}$ in the three-dimensional domain is then constructed by summing the sine and cosine series with random phases and amplitudes (Huang *et al.* 2010)

$$v_i(\bar{x}, t) = \sqrt{\frac{2}{N}} \sum_{n=1}^N [p_i^n \cos(\tilde{\kappa}_j^n \tilde{x}_j + \omega_n \tilde{t}) + q_i^n \sin(\tilde{\kappa}_j^n \tilde{x}_j + \omega_n \tilde{t})] \tag{3}$$

where

$$\begin{cases} \tilde{x}_j = \frac{x_j}{l}, \quad \tilde{t} = \frac{t}{\tau}, \quad \tilde{\kappa}_j^n = \kappa_j^n \frac{c}{c_{(j)}}, \quad c = \frac{l}{\tau}, \quad p_i^n = \varepsilon_{ijm} \xi_j^n \kappa_m^n, \quad q_i^n = \varepsilon_{ijm} \xi_j^n \kappa_m^n \\ \xi_i^n \in N(0,1), \quad \xi_i^n \in N(0,1), \quad \omega_n \in N(0,1), \quad \kappa_i^n \in N(0,1/2) \end{cases} \tag{4}$$

In Eqs. (3) and (4), ε_{ijk} is the permutation tensor used in the vector product operation, $N(M, \sigma)$ is a random variable following a normal distribution, with a mean of M and standard deviation of σ (i.e., $\xi_i^n \in N(0,1)$ means that ξ_i^n follows a normal distribution with mean of 0 and standard deviation of 1), l and τ are the length and time-scales of the turbulence, which can be calculated from the turbulent kinetic energy k and the turbulent dissipation rate ε or determined based on experimental results. κ_j^n and ω_n are the values of the spatial and temporal power spectral densities at discrete points, calculated as follows

$$E(k) = 16(2/\pi)^{1/2} \kappa^4 \exp(-2\kappa^2) \tag{5}$$

Finally, the target turbulent fluctuating wind field u_i is generated by applying a scaling and orthogonal transformation to the transient flow field v_i obtained in the previous step

$$w_i = c_{(i)} v_{(i)} \tag{6}$$

$$u_i = a_{ik} w_k \tag{7}$$

Eqs. (6) and (7) mathematically express the scaling and orthogonal transformation respectively. Both the scaling factors c_i and the transformation tensor a_{ij} , which are time-independent, can be calculated using Eq. (1) through an efficient matrix diagonalization routine.

According to the orthogonality relationship between κ_i^n and p_i^n, q_i^n is $\kappa_i^n p_i^n = \kappa_i^n q_i^n = 0$. In addition, when the derivatives of c_i are neglected,

$$w_{i,i} = c_{i,i} v_i + c_i v_{i,i} \approx c_{i,i} v_{i,i} = \frac{c}{l} \sqrt{\frac{2}{N}} \sum_{n=1}^N \left[-p_i^n \kappa_i^n \sin\left(\frac{c}{c_j} \kappa_j^n \frac{x_j}{l} + \omega_n \frac{t}{\tau}\right) + q_i^n \kappa_i^n \cos\left(\frac{c}{c_j} \kappa_j^n \frac{x_j}{l} + \omega_n \frac{t}{\tau}\right) \right] = 0 \tag{8}$$

Eq. (8) is exact for homogeneous turbulence and hence the flow field w_i generated after the scaling transformation is divergence free under the homogeneous condition. Combining Eq. (8) and the transformation characteristics of the derivatives, i.e., $f'_i = a_{ij} f'_j$, the divergence-free property of the flow field can be preserved by the orthogonal transformation, as expressed by Eq. (7)

$$u_{i,i} = a_{ij} a_{ki} w_{j,k} = \delta_{jk} w_{j,k} = w_{j,j} = 0 \tag{9}$$

After the transformation, the resulting generated flow field satisfies the anisotropic requirement of the original flow field, i.e.

$$\overline{u_i u_j} = \overline{a_{im} w_m a_{jn} w_n} = a_{im} a_{jn} c_m c_n \overline{v_m v_n} = a_{im} a_{jn} \delta_{mn} (c_n)^2 = r_{ij} \quad (10)$$

In conclusion, the generated flow field $u_i(\bar{x}, t)$ is transient, divergence-free, inhomogeneous, and anisotropic with the prescribed statistical characteristics.

Obviously, the length- and time-scales (l, τ) of the turbulence are important to allow the RFG technique to generate a realistic fluctuating velocity field (Huang *et al.* 2010). A parametric study comparing three turbulence length scale models, namely L given in Smirnov *et al.* (2001), L and $C_L L$ given in Huang *et al.* (2010), was conducted by Huang *et al.* (2010) and the results indicated that the spatial correlation coefficient decreases with the increase of distances when l is used. In contrast, a relatively good agreement with the theoretical exponent function has been found when L or $C_L L$ ($C_L = 1.5$) is used, especially when $C_L L$ was used (see Fig. 1). Since the length scale adjusts the spatial correlation coefficient between two given points, choosing a proper length scale model is important for obtaining a turbulent fluctuating velocity field with the prescribed spatial correlation coefficient. However, no specific calculation method or selection principle for obtaining the length scale L was given in the study by Huang *et al.*

In fact, the turbulent length- and time scales (l, τ) can be calculated from the turbulence kinetic energy κ and the turbulence dissipation rate ε , or determined based on experimental data. The length scale calculation $l = (C_\mu)^{0.75} k^{1.5} / \varepsilon$ was used in Smirnov *et al.* (2001), where $k = 3/2(IU_{avg})^2$ and $\varepsilon = a^{-1.5} \kappa^{5/2} E_u(\kappa)^{3/2}$ (I is the turbulence intensity, U_{avg} is the averaged velocity, κ is the wave length in the inertial subrange, $E_u(\kappa)$ is energy spectral intensity, and $a = 0.5-0.6$). Although the calculation of the length- and time-scales adopted in Smirnov's study ensures the power spectra of the generated random flow field agrees well with the Gaussian model, it deviates from the von Karman spectrum model (Huang *et al.* 2010). The generated fluctuating velocity field, however, is considered to be more realistic for wind engineering applications if the power spectrum of the generated fluctuating velocity field agrees with the von Karman model according to the conclusions from previous studies (Li *et al.* 2004, 2005, 2007). Therefore, a method which combines the calculations of the turbulent kinetic energy k and the dissipation rate with the RFG technique would significantly improve the generation of the random flow field in terms of providing more realistic length- and time-scales for the turbulence. Consequently, the power spectra of the generated fluctuating velocity field would agree with the widely adopted von Karman model.

3. Combination method of calculating the turbulence properties

Modelling the equilibrium Atmospheric Boundary Layers (ABL) in the framework of Computational Fluid Dynamics (CFD) is an important precondition to numerically solve the boundary-layer-related flow problems, such as investigations on the wind effect on buildings, the simulation of open channel transportations etc. Simulating an equilibrium boundary layer was investigated by Yang *et al.* (2009) from the view-point of the widely adopted two equation turbulence model. Based on the local equilibrium assumption, Yang *et al.* (2009) theoretically derived solutions to the k equation based on the equations adopted in the standard $k-\varepsilon$ model, as well as in the SST $k-\varepsilon$ model, and then proposed a new set of the turbulent inflow boundary

conditions for k and ε . It has been numerically verified that the inflow boundary conditions produce an equilibrium ABL in the Reynolds-averaged Navier-Stokes simulation (Yang *et al.* 2008, 2009, Tse *et al.* 2013). Recently, the performance and applicability of the proposed set of the inflow boundary conditions have been validated (Gorlé *et al.* 2010, O'Sullivan *et al.* 2011) and have been adopted in the numerical simulations of ABL flows (Barić *et al.* 2010, Kozmar 2011, Labovský and Jelemenský 2011, Parente *et al.* 2011).

The transport equations of k and ε in the framework of the k - ε turbulence model for a steady, incompressible and horizontally homogeneous flow read (Jones and Launder 1972)

$$\frac{C_\mu}{\sigma_k} \frac{\partial}{\partial z} \left(\frac{k^2}{\varepsilon} \frac{\partial k}{\partial z} \right) + C_\mu \frac{k^2}{\varepsilon} \left(\frac{\partial u}{\partial z} \right)^2 - \varepsilon = 0 \quad (11)$$

$$\frac{C_\mu}{\sigma_\varepsilon} \frac{\partial}{\partial z} \left(\frac{k^2}{\varepsilon} \frac{\partial \varepsilon}{\partial z} \right) + C_{1\varepsilon} C_\mu k \left(\frac{\partial u}{\partial z} \right)^2 - C_{2\varepsilon} \frac{\varepsilon^2}{k} = 0 \quad (12)$$

and were used to derive the inflow turbulent boundary conditions of k and ε as proposed by Yang *et al.* (2009, 2012). In Eqs. (11) and (12), C_μ , σ_k , σ_ε , $C_{1\varepsilon}$, $C_{2\varepsilon}$ are constants, and k and ε are the turbulent kinetic energy and dissipation rate, respectively. Assuming that the turbulence production and dissipation are in a local equilibrium condition, the turbulence dissipation rate ε can be expressed as

$$\varepsilon = \sqrt{C_\mu} k \frac{\partial u}{\partial z} \quad (13)$$

Substituting Eq. (13) into Eq. (11) yields

$$\frac{C_\mu}{\sigma_k} \frac{\partial}{\partial z} \left(\frac{k^2}{\varepsilon} \frac{\partial k}{\partial z} \right) = 0 \quad (14)$$

As C_μ and σ_k are constants, the transport equation of k is reduced as

$$\frac{\partial}{\partial z} \left(\frac{k^2}{\varepsilon} \frac{\partial k}{\partial z} \right) = \frac{\partial}{\partial z} \left(\frac{kk'(z+z_0)}{u^* z_0 \sqrt{C_\mu}} \frac{\partial k}{\partial z} \right) = 0 \quad (15)$$

When a logarithmic mean wind profile is used (Simiu and Scanlan 1996)

$$u = \frac{u^*}{k'} \ln \left(\frac{z+z_0}{z_0} \right) \quad (16)$$

Eq. (13) can be rewritten as

$$\varepsilon = \frac{ku^* \sqrt{C_\mu}}{k'} \frac{z_0}{z+z_0} \quad (17)$$

In expression (16), u^* is the friction velocity, k' is the von Karman constant and z_0 is the aerodynamic roughness length. Combining Eqs. (12), (16) and (17), the transportation equation of ε is reduced to

$$\left(\frac{\partial k}{\partial z}\right)^2 + k \frac{\partial^2 k}{\partial z^2} + \frac{k^2}{(z+z_0)^2} - \frac{2k}{z+z_0} \frac{\partial k}{\partial z} + \frac{k\sigma_\varepsilon(u^*)^2}{(k')^2} \frac{(C_{1\varepsilon} - C_{2\varepsilon})z_0^2}{(z+z_0)^2} = 0 \tag{18}$$

According to Eq. (15), the vertical variation of k can be solved from

$$\frac{kk'(z+z_0)}{u^*z_0\sqrt{C_\mu}} \frac{\partial k}{\partial z} = A \tag{19}$$

where A is a constant. Eq. (19) is a linear first-order differential equation, which has the following solution

$$k = \sqrt{D_1 \ln\left(\frac{z+z_0}{z_0}\right) + D_2} \tag{20}$$

where D_1 and D_2 are constants that describe the inflow turbulence level. Eq. (20) shows that k is a nonlinear function of the height above ground z and is the analytical solution to the transport equation for k . Before adopting Eq. (20) as the inflow boundary condition for k , a simple linear transformation for the constants D_1 and D_2 is performed

$$D_1 = \left(\frac{u_*^2}{\sqrt{C_\mu}}\right)^2 C_1, \quad D_2 = \left(\frac{u_*^2}{\sqrt{C_\mu}}\right)^2 C_2 \tag{21}$$

C_1 and C_2 can be determined by nonlinear fitting of Eq. (20) with experimental data for k . Combining Eqs. (20) and (21) yields

$$k = \frac{u_*^2}{\sqrt{C_\mu}} \sqrt{C_1 \ln\left(\frac{z+z_0}{z_0}\right) + C_2} \tag{22}$$

Substituting Eq. (22) into Eq. (17) yields,

$$\varepsilon = \frac{u_*^3}{k'(z+z_0)} \sqrt{C_1 \ln\left(\frac{z+z_0}{z_0}\right) + C_2} \tag{23}$$

In conclusion, combining the RFG technique articulated in section 2 and the calculations of k and ε presented in this section (i.e., Eqs. (21) and (22)), which are used to estimate the length- and time-scales (l, τ) of the target fluctuating turbulence field, the time-dependent turbulent fluctuating velocity field can be generated as the inflow boundary conditions in a LES simulation.

4. Validation of the CRFG technique

In order to verify the reliability of the CRFG technique established in the present study, the computational models investigated by Gousseau *et al.* (2013) were adopted and studied for the purpose of comparison and verification. The computational domain, model dimensions, grid generation and the numerical schemes from the study of Gousseau *et al.* (2013) are used. As

regards the boundary conditions, the building and ground surfaces, top-, side- and outlet-boundaries of the domain are specified following the work of Gousseau *et al.* (2013). The inlet-boundary of the domain is, however, specified using the CRFG technique proposed in section 3. A brief description of the computational model is given in the following and more details can be found in the study of Gousseau *et al.* (2013).

Computational domain and grid: the domain dimensions are 2.64 m×0.9 m×0.9 m (see Fig. 2), which is slightly below the recommendations by COST Action 732 (Franke *et al.* 2007) and AIJ (Tominaga *et al.* 2008) guidelines in order to limit the deterioration of the prescribed inflow profiles along the empty fetch upstream of the building (Blocken *et al.* 2007a, b). Two sets of computational grids, Grid20 (with a total number of computational cells of 737,920) and Grid30 (with a total number of computational cells of 2,504,160), are adopted for comparison purposes.

Boundary conditions: the boundary conditions are specified as shown in Fig. 2. It is worth mentioning that the Vortex Method (VM) (Sergent 2002, Mathey *et al.* 2006) is used to generate the inlet velocity profile of the computational domain in the study of Gousseau *et al.* (2013).

Numerical schemes: the convection term is discretized using a bounded central-differencing scheme in the filtered momentum equation. The second-order implicit scheme is adopted for time discretization and a non-iterative scheme is used for time advancement. The time-step of the Grid20 scheme is 0.0008s and for the Grid30 scheme is 0.000533s.

Random perturbations were superimposed onto proceeding RANS simulation results to initialize each simulation (Grid20 and Grd30). The turbulence statistics were then sampled from the LES simulation results. To facilitate the discussion in the following subsections, different simulations with different inflow boundary condition are abbreviated as,

- CRFG: Grid20 for computational grid, standard Smagorinsky, CRFG inlet flow generation method and constant $C_s = 0.1$ is considered.
- RFG: Grid20 for computational grid, standard Smagorinsky, RFG inlet flow generation method and constant $C_s = 0.1$ is considered.
- Exp: Experimental data from Gousseau *et al.* (2013);
- LES20-1: Grid20 for computational grid, standard Smagorinsky, VM inlet flow generation method and constant $C_s = 0.1$ is considered;
- LES30-1: Grid30 for computational grid, standard Smagorinsky, VM inlet flow generation method and constant $C_s = 0.1$ is considered.

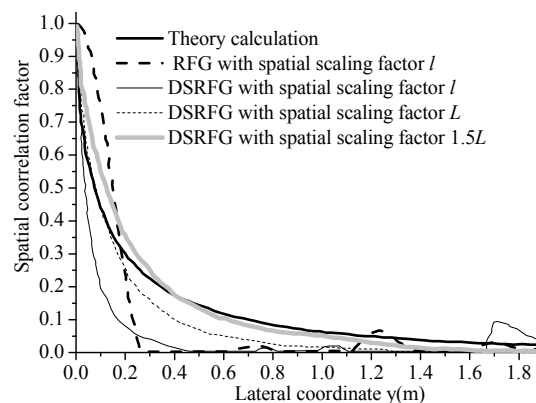


Fig. 1 Comparison of spatial correlation with different length scales

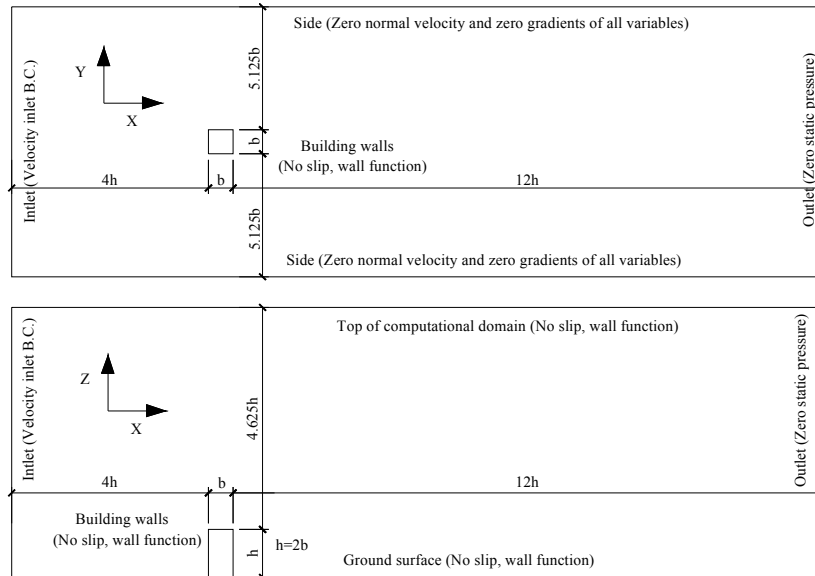


Fig. 2 Computational domain and boundary conditions

4.1 Comparison between CRFG and RFG

Several time-series of the fluctuating wind velocities generated by the LES with the inflow boundary conditions specified using the CRFG technique and the RFG technique are displayed in Fig. 3 to illustrate the differences between these two methods. Fig. 4 shows the power spectral density curves generated by the CRFG and the RFG simulations in a comparison with the target von Karman spectrum. Fig. 5 shows the comparisons of the calculated spatial correlation based on different LES results and theoretical models with different spatial scaling factors. As is evident in these figures, the power spectral density obtained from the CRFG simulation is in a good agreement with the target von Karman spectrum throughout the frequency range under investigation. This agreement is of great importance in the field of wind engineering as the power spectral density of the generated fluctuating velocity field obeys a realistic turbulence spectrum model observed in natural winds. Given the non-negligible effect of the wind-induced fluctuating forces acting on buildings and structures with frequencies in the inertial sub-range, the accurate and reliable reproduction of the target power spectral density at relatively high frequency ($fL/V(z)) > 0.1$) is important in simulating the wind effects on structures (Li *et al.* 2005, 2007). Good agreement is also found in the comparison of the spatial correlation coefficients (calculated based on the CRFG simulation and the target decreasing curve).

In contrast, the power spectral density calculated from the RFG simulation results deviates from the theoretical predictions. This can be explained as follows. Since the length- and time-scales are very important in order that the generated fluctuating velocity field is realistic as they determine the statistics of the generated fluctuating velocity field (Huang *et al.* 2010). The consistent frequency zone within which the power spectral density curve calculated from the RFG simulation results agrees with the von Karman model at the low frequency end. When the

frequency increases, the power spectral density curve calculated from the RFG simulation results decays more rapidly than the von Karman model prediction. When using the RFG technique to generate the fluctuating velocity field used for the inflow boundary conditions, a Gaussian model is assumed, which was designed originally to describe the energy-containing sub-range turbulence fluctuations. As the energy-containing sub-range frequently concentrates at the low frequency end, the turbulence energy contained in the inertial and dissipation sub-ranges, which are commonly found at the high frequency end, are not reliably described by the Gaussian model, and therefore the fluctuating velocity field generated by the RFG technique is not realistic in terms of the turbulent kinetic energy distribution at the high frequency end. In fact, the generated random fluctuating wind field is caused by a type of initial disturbance rather than real turbulence eddies (Schluter *et al.* 2004). As a result, the presented CRFG method with M1 mesh scheme provides a feasible and reliable way of generating turbulent fluctuating wind fields, which satisfies the required turbulence characteristics, such as power spectrum intensity and spatial correlation factor. As the power spectral density curve of the fluctuating velocity field generated by the CRFG technique agrees with the realistic von Karman model, the CRFG technique is used to generate the inlet fluctuating velocity field in the following simulations.

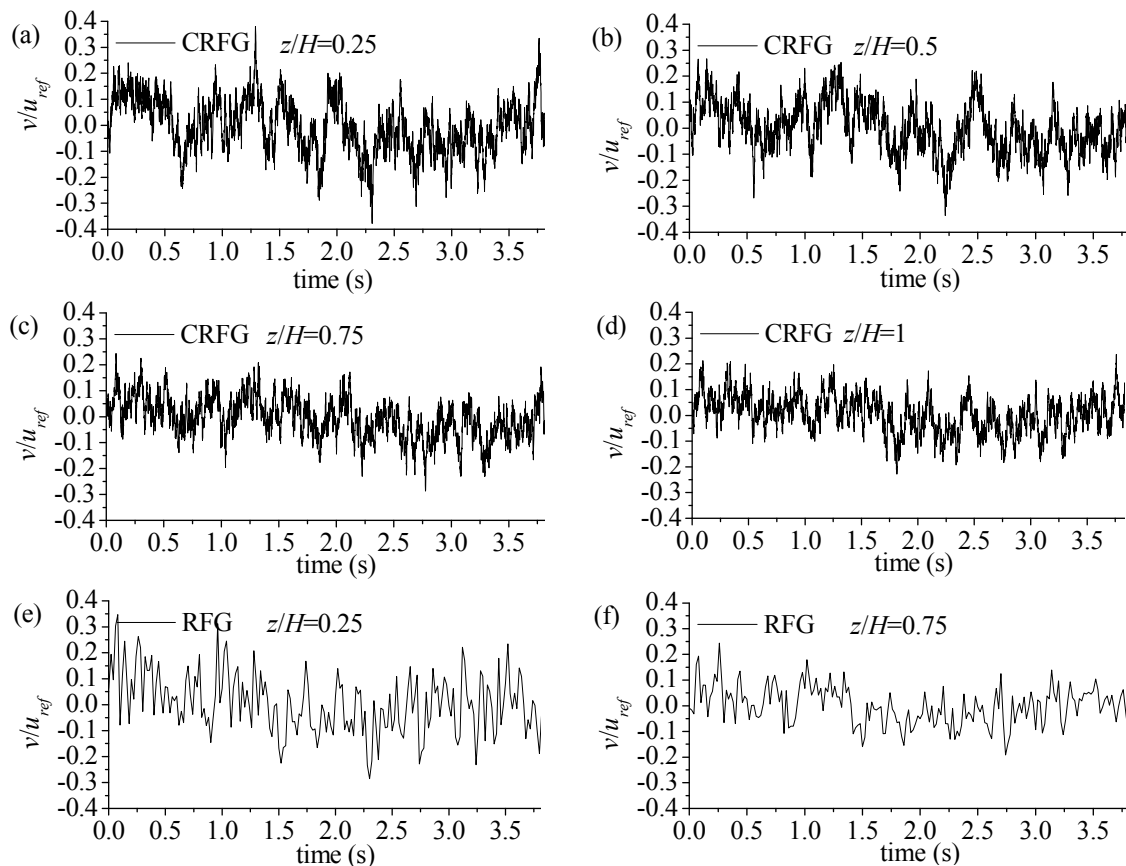


Fig. 3 Samples of fluctuating wind velocity time-series: (a) $z/H = 0.25$ (CRFG), (b) $z/H = 0.5$ (CRFG), (c) $z/H = 0.75$ (CRFG), (d) $z/H = 1$ (CRFG), (e) $z/H = 0.25$ (RFG) and (f) $z/H = 0.75$ (RFG)

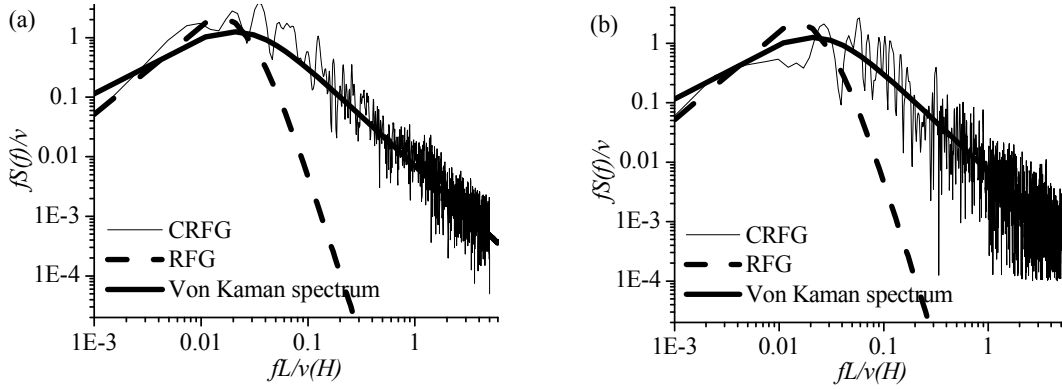


Fig. 4 Comparison of power spectrum between theory and simulation: (a) $z/H = 1.0$ and (b) $z/H = 0.25$

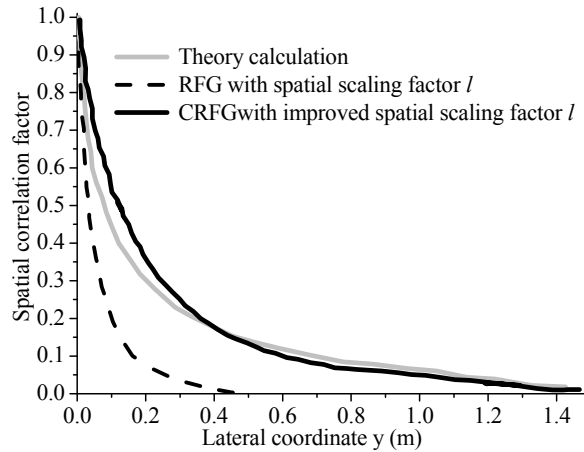


Fig. 5 Comparison of spatial correlation factor

4.2 Comparison validation between CRFG and existing study results

Comparison of inlet non-dimensional stream-wise velocity and turbulent kinetic energy profiles calculated based on the results of Exp, LES20-1, LES30-1 and CRFG are shown in Fig. 6. The experimental and numerical profiles of the non-dimensional mean stream-wise velocity and the turbulent kinetic energy at the position of $y/b = 0$ are shown in Fig. 7. Good agreement among the inflow velocity profiles calculated based on the results of Exp, LES20-1, LES30-1 and CRFG is clearly shown in Fig. 6(a), which verifies LES as providing reliable estimates of the vertical variation of the wind velocity when the CRFG technique is applied to generate the turbulent fluctuations at the inlet boundary. Similarly, a good agreement among the non-dimensional mean stream-wise velocity profiles calculated based on the results of Exp, LES20-1 and LES30-1 and CRFG is observed for the profiles at the locations of $x/b = -0.75; -0.25; 0.5; 1.25; 3.25$ in Fig. 7(a).

However, as for the vertical profiles of the non-dimensional turbulent kinetic, the agreement as good as that shown in Figs. 6(a) and 7(a) is not observed in Figs. 6(b) and 7(b) for the profiles

calculated based on numerical and experimental data. More importantly, the profile calculated based on the CRFG simulation deviates from the calculated profile based on experimental data to a noticeable extent. The differences between the calculated profiles based on the results of Exp and LES20-1/LES30-1 are actually larger or similar to the differences between the calculated profiles based on the results of Exp and CRFG. It has been discovered by Gousseau *et al.* (2013) that it is a common phenomenon that the turbulent kinetic energy profile calculated from the numerical simulation results may deviate from the measurements taken in wind tunnel tests. In fact, the study of Gousseau *et al.* (2013), and other previous works (Murakami 1993, Meng and Hibi 1998, Celik *et al.* 2005) have shown that a coarse grid may get a better agreement, when compared to a refined grid system, between the numerically simulated and the wind tunnel measured turbulent kinetic energy. Measurement bias in the velocity fluctuations obtained in the wind tunnel tests and differences in the sampling frequency may also be possible explanations for the discrepancy between numerically simulated and the wind tunnel measured turbulent kinetic energy.

In summary, comparative analysis between the numerical simulation results of CRFG, LES20-1/LES30-1 and the wind tunnel experimental data shows that the LES simulated wind field around a bluff body acceptably agrees with the experimental results obtained from the wind tunnel tests, thereby validating the approach used. Therefore, it can be concluded that the fluctuating velocity field generated by the CRFG technique is suitable for determining the inflow boundary conditions in a LES. The CRFG technique is hence adopted to study the flow field around irregular buildings in the following sections.

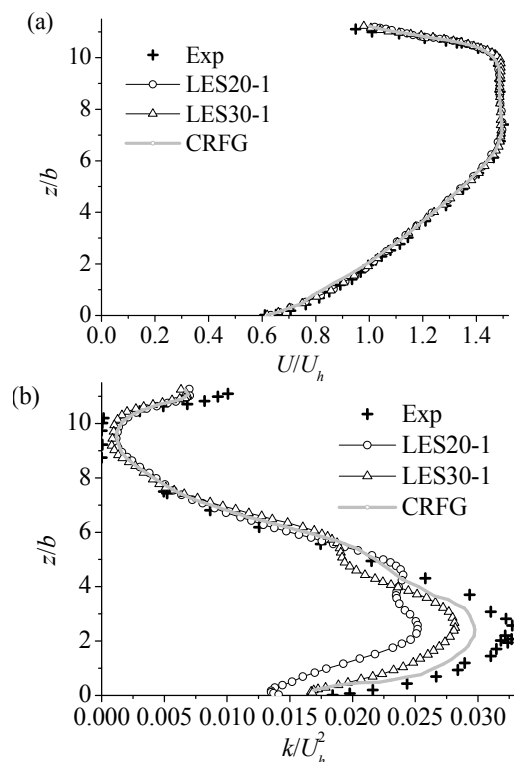


Fig. 6 Inlet profiles between experiment and numerical results averaged in the lateral direction: (a) non-dimensional inlet velocity and (b) non-dimensional turbulent kinetic energy

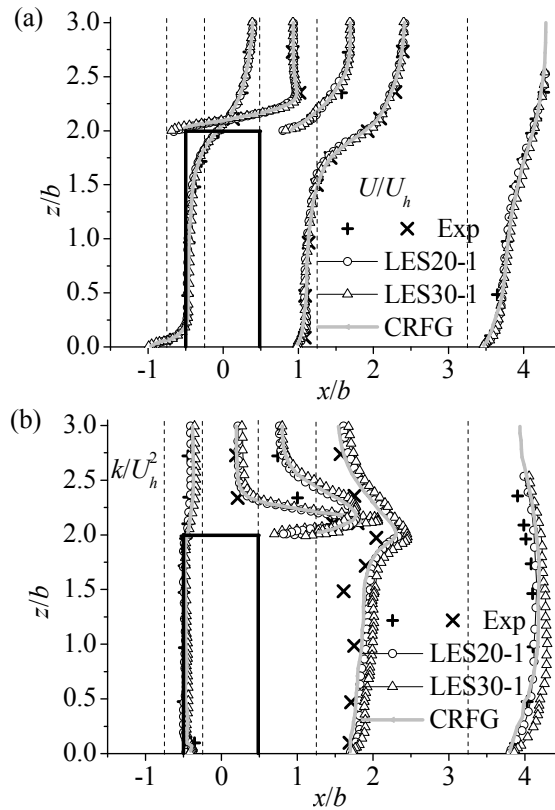


Fig. 7 Experimental and numerical profiles of (a) non-dimensional mean stream-wise velocity and (b) turbulent kinetic energy in the plane V0 ($y/b = 0$)

5. Application of the CRFG technique

5.1 Computational model

As mentioned in section 3, a random fluctuating velocity field with a spectrum following the von Karman model or other reasonable models describing the spectral characteristics of natural winds is of great importance in computational wind engineering applications as it can be used to specify the inflow boundary conditions in a LES. In this section, a series of LES on wind flows around four irregularly-shaped buildings are reported. In detail, the wind-flow around four high-rise buildings (S-, R-, L- and U-shaped in the horizontal plane) models with a geometric scale of 1:200 were simulated by LES. The building models and their dimensions are shown in Fig. 8 and Table 1 respectively. Both structured and unstructured grids were used for the mesh generation, as shown in Fig. 9. The Reynolds numbers calculated based on the width L and $v(H)$ (inflow velocity at a height of $z = H$) were in the range from 6.7×10^5 to 1.4×10^6 , which implies that finer grid resolutions are needed near the building model surface for the boundary layer regions. Therefore, unstructured meshes were generated for the zones near the bluff body surface, and structured meshes were applied to discretize the space outside the unstructured meshes. The

ADINA (2005) platform was adopted for the numerical simulation, which has the capacity of dealing with both the structured and unstructured grids. The average non-dimensional distance y^+ of the first layer of grids from the surface was about $L/5000$ in the X direction and about $B/5000$ in the Y direction, which is smaller than the values suggested by Murakami (Murakami 1998) ($D/1000$) and Huang (Huang 2006) ($D/4000$). More specifically, all the y^+ values in the simulations were approximately found to be in the range of [3.5, 92.4]. The Reichardt wall-law was used to determine the shear stresses at the wall surface (Camarri *et al.* 2002). The total number of cells of the computational domain was about 7,000,000 and the cell size was increased by a factor of 1.1 to limit the commutation error. Tetrahedral elements, generated using a free-form mesh generator for complicated geometries and capable of dealing with high Reynolds number flows, were used in the boundary layer region.

The inflow boundary condition was specified by adding the mean wind profile described by the logarithmic law and the turbulent fluctuating wind velocities generated using the CRFG technique. For the outflow boundary, the convective boundary condition was applied for velocity and pressure, i.e., $\partial/\partial t + c(\partial/\partial x) = 0$, where c is the bulk velocity to ensure global mass conservation. A slip condition was assumed for the velocities on the two lateral sides and the top of the computation domain, which means $\partial U/\partial y = \partial U/\partial w = V = W = 0$ at these slip boundaries. The non-slip condition was used for the velocities on the ground surface, i.e., $u_n = 0$. The Neumann condition was employed to calculate the pressure on building surfaces which means that the pressure gradient perpendicular to the surfaces was zero.

The simulations were performed on a supercomputer with 16 processors (2.6 GHz; 32 GB memory). The numerical time step was 5×10^{-5} s and 100,000 steps were needed to collect data for determining the computational stability, which give a total time length of the simulation of 5s. Each case was simulated with a premature process in which all initial transient conditions were washed out. The premature simulation needed about 25,000 time steps in this study, after which a semi-steady state operating state was reached (Farzad *et al.* 2013). Time averaging was then begun so as to obtain acceptable statistical convergence results for all the relevant quantities (such as velocity and concentration).

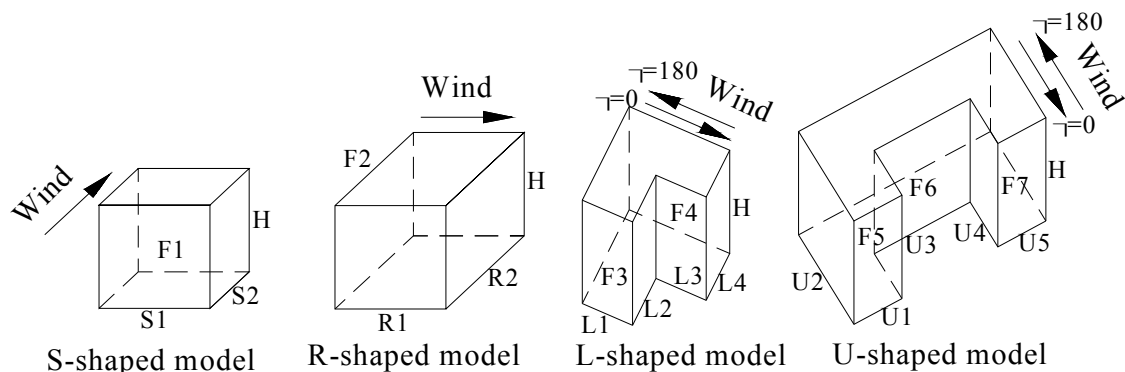


Fig. 8 Computational models

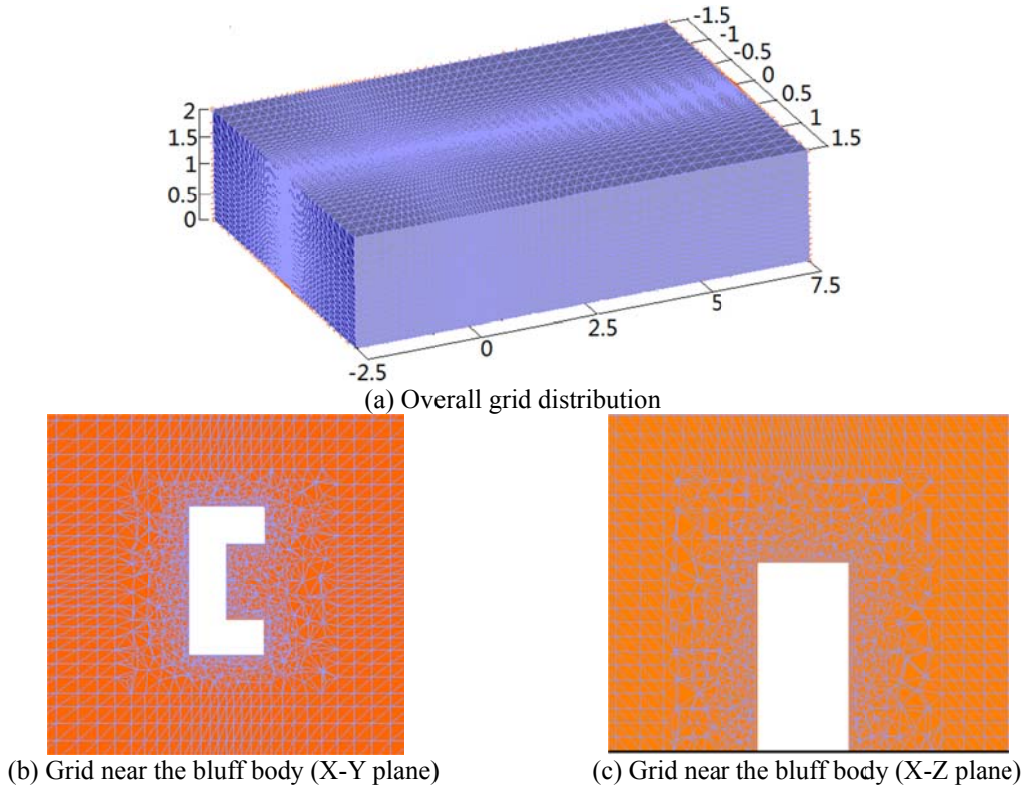


Fig. 9 Grid generation style

5.2 Distribution of mean and fluctuating pressure coefficients

Studies on the mean pressure coefficient distribution on the surfaces of a bluff body have been conducted by many researchers (such as: Gomes 2005, Huang 2006, Wang 2010, 2011, Sepe and Marcello 2014, Tunay *et al.* 2013, Dagneu and Bitsuamlak 2014). Gomes *et al.* (2005) investigated the results of a series of wind tunnel tests on the distribution of the pressure acting on L- and U-shaped models and presented some important results. Important parameters concerning the pressure acting on the building models, such as the location of the peak mean pressure coefficient and the fluctuating pressure coefficient, were not included in the report of Gomes *et al.* (2005). Huang *et al.* (2006), on the other hand, focused on the mean/fluctuating pressure coefficients and the wind velocity field around the CAARC building model. The main content of the study was a comparative analysis on the pressure coefficient distribution on the surfaces of the different kinds of bluff bodies. More specifically, the study obtained some meaningful conclusions on the locations of the peak mean pressure coefficient and the change tendency of the wind pressure on different body surfaces. The conclusions provide referential information on the wind pressure on regularly and irregularly shaped bluff bodies. Pressure data obtained from computational simulation is processed using equations as shown in Table 2.

Table 1 Model dimensions (m)

S-shaped model	$S1 \times S2 \times H$	R-shaped model	$R1 \times R2 \times H$
Case A	$1 \times 1 \times 1$	Case B	$1 \times 0.5 \times 1$
L-shaped model	$L1 \times L2 \times L3 \times L4 \times H$	U-shaped model	$U1 \times U2 \times U3 \times U4 \times U5 \times H$
$\alpha = 0^\circ$ $\alpha = 180^\circ$		$\alpha = 0^\circ$ $\alpha = 180^\circ$	
Case C Case D	$0.5 \times 0.5 \times 0.5 \times 0.5 \times 1$	Case E Case F	$0.5 \times 1 \times 1 \times 0.5 \times 0.5 \times 1$

Table 2 Data processing equations

Wind pressure coefficient	$C_{pi}(n) = \frac{p_i(n)}{\rho U_{ref}^2 / 2} \quad (n = 1L N)$
Mean wind pressure coefficient	$\bar{C}_{pi} = \sum_{n=1}^N \frac{C_{pi}(n)}{N}$
Fluctuating wind pressure coefficient	$C_{pi,rms} = \sqrt{\frac{\sum_{n=1}^N (C_{pi}(n) - \bar{C}_{pi})^2}{N-1}}$

Note: i is the number of pressure tap; N is the sample length of the wind pressure time series; $\rho = 1.2 \text{ kg/m}^3$ is air density; U_{ref} is wind velocity at height of H

The mean pressure coefficients produced by the numerical simulations with the inflow boundary condition specified using the CRFG/RFG/DES (detached-eddy simulation) techniques and calculated based on the wind tunnel test results are shown in Fig. 10. The measurement section of the wind tunnel has dimensions of 10 m (length) \times 3 m (width) \times 2 m (height), in which the maximum wind velocity is 20 m/s (Tse *et al.* 2012). The reference wind velocity in the approaching wind flow was 8.3 m/s, and the sampling frequency was 313 Hz. Roughness elements were arranged to make the approaching wind flow employed in the wind tunnel tests fall into the type B category as defined in the loading code for the design of building structures of China (China Ministry of Construction 2012), which corresponds to a suburban environment. As shown in Fig. 10, the differences between mean pressure coefficients produced by the numerical simulations and those calculated based on the wind tunnel test results are reasonably small, although there are some noticeable discrepancies. These discrepancies, however, are negligible in comparison with the variation of the pressure coefficient itself. The discrepancies, on the other hand, can be explained as follows: (a) the numerical and experimental settings are not exactly the same when the model boundary conditions, turbulence intensities and blocking effects are of concern, and (b) the mean pressure coefficients on the side and back faces of the building model are sensitive to the turbulence intensity, as discussed by Huang *et al.* (2010). When compared with the numerical simulation results of either the DES or the RNG-LES, the CRFG-LES results are more satisfactory in terms of agreement with the wind tunnel test results. Consequently, the comparison shown in Fig. 10 substantiates the turbulent fluctuating velocity field generated using CRFG technique as reliable.

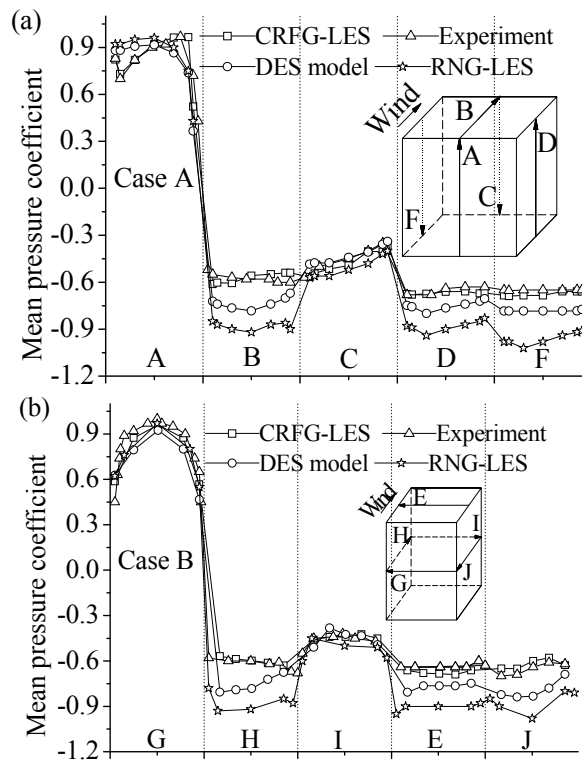


Fig. 10 Comparison of mean pressure coefficients: (a) Case A and (b) Case B

Fig. 11 shows the curves of mean pressure coefficients on the front faces for all the cases, and the mean pressure coefficients on the front, side, roof and rear faces for case E, and those of case F are presented in Fig. 12. The vertical variations of the mean pressure coefficients shown in Fig. 11 indicate that the mean pressure acting on the front face of a bluff body is reduced initially at the lower levels ($z/H < 0.2$) and then increases with the height at the medium levels ($0.3 < z/H < 0.8$). The minimum pressure coefficient occurs at a height of approximately $H/4$ from the ground. At high levels of the building ($z/H > 0.8$), the mean pressure coefficient decreases with increasing height. The maximum pressure coefficient occurs at a height of approximately $4H/5$. The lateral variation of the mean pressure coefficients on the front faces, on the other hand, shows a gradual decrease from the center to both side faces. Maximum mean pressure coefficients appear along the center line of the front faces. This suggests that the influence of bluff body on the flow field along the centerline of the building is more obvious than in the region near the side faces. The mean pressure coefficients on the roof, side and rear faces are all negative and complicated pressure distributions are observed for these regions, which suggests that all of these faces are suction faces on which asymmetric generation and shedding of vortices occur.

Comparisons between the fluctuating pressure coefficient contours calculated from the wind tunnel test results and from the numerical simulation results for case A and case B are shown in Fig. 13, which indicate that the fluctuating pressures obtained from the numerical simulations agree well with the wind tunnel test results. This substantiates the use of the CRFG technique for

generating a reliable fluctuating velocity field for use as an inflow boundary condition in a LES. This focuses on predicting the fluctuation of the pressures acting on the irregularly-shaped bluff body induced by the interaction between the transit wind flow and the steady bluff body model.

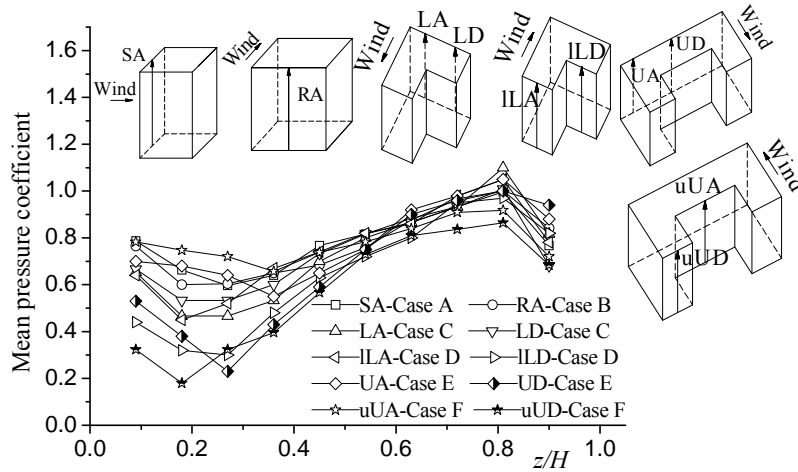


Fig. 11 Mean pressure coefficient curves on front faces

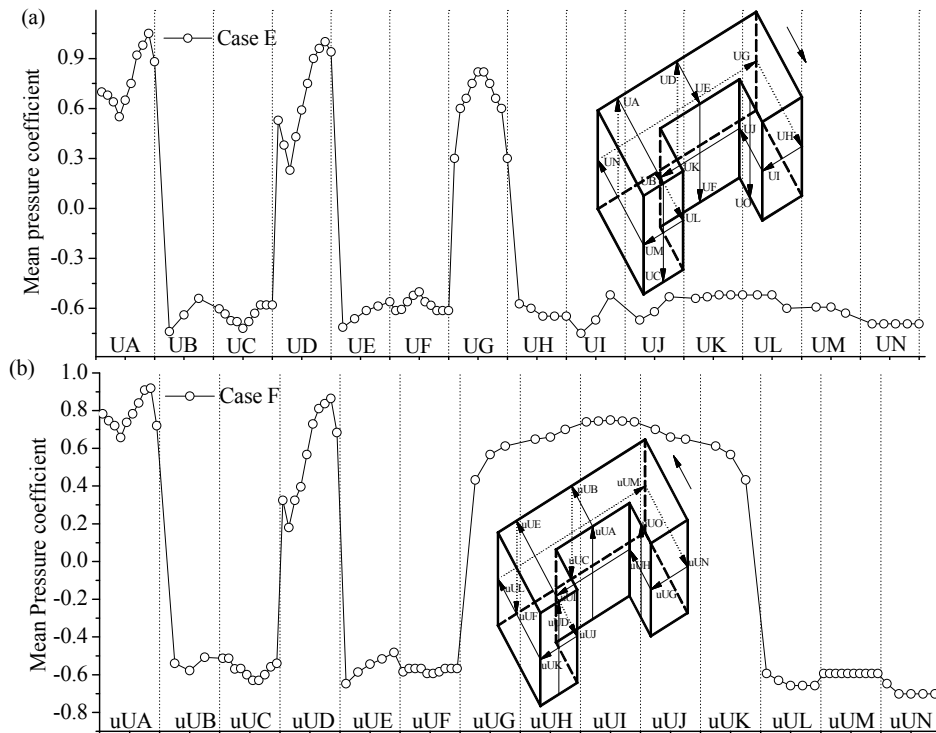


Fig. 12 Mean pressure coefficients: (a) Case E and (b) Case F

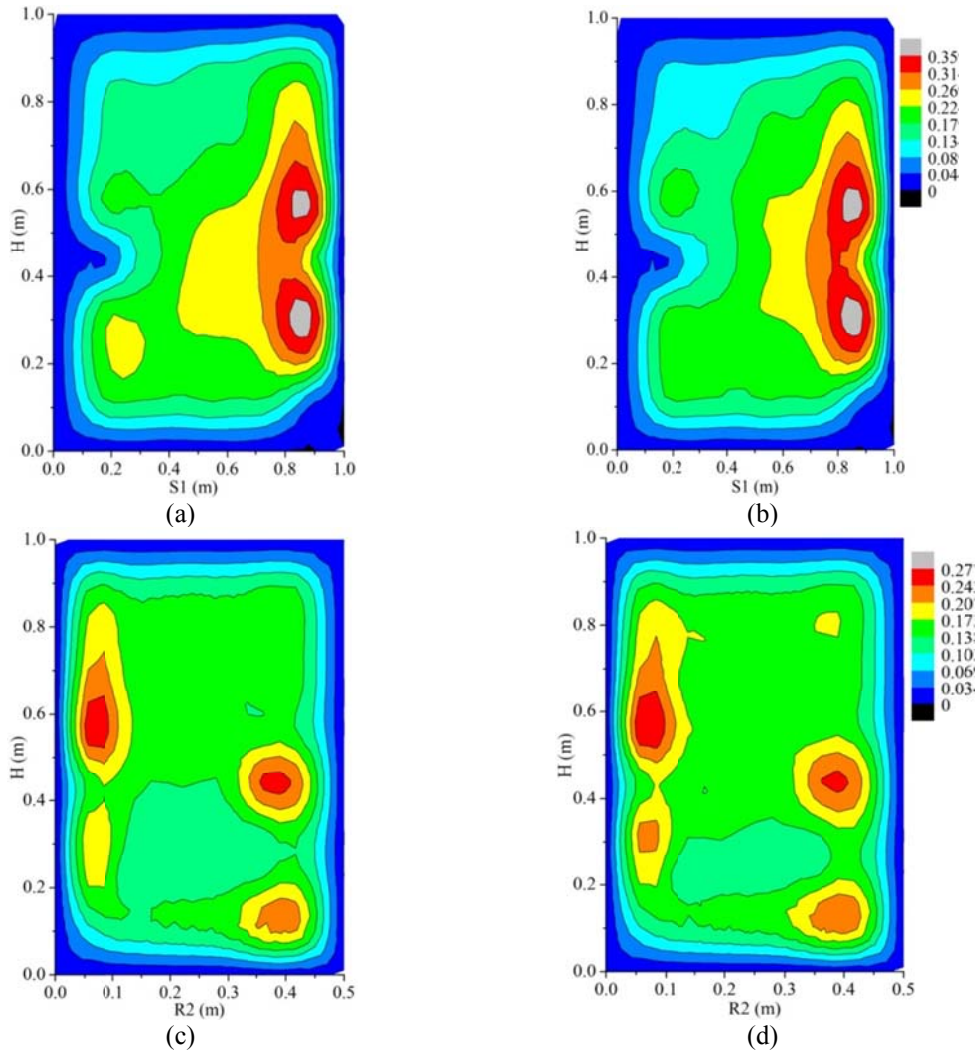


Fig. 13 Fluctuating pressure coefficient contours: (a) case A, side face and wind tunnel test, (b) case A, side face and numerical simulation, (c) case B, back face and wind tunnel test and (d) case B, back face and numerical simulation

Fig. 14 shows the fluctuating pressure coefficient contours on the side, back and front faces for cases C, D, E and F. The fluctuating pressure coefficients on the side faces are larger than those on the front and back faces, especially at the flow separation locations, which indicates that the fluctuating pressure coefficients are greatly influenced by the vortex behavior. More specifically, strong vortex movements induce great vortex energy, which in turn induce large fluctuating pressure coefficients. Therefore, it can be concluded that the fluctuating pressure coefficients have a similar distribution to the mean pressure coefficients, i.e., large fluctuating pressure appears at the places where large negative mean pressure coefficients are found, and vice versa. This is due to

the large fluctuating pressure coefficients and large negative mean pressure coefficients being directly caused by the vortex movements. On the back face of the building, the vortex motion is chaotic and the energy is relatively small when compared to the vortex movements on the side faces. As a result, the fluctuating pressure coefficients on the back faces are smaller than those on side faces. In addition, as shown in Fig. 14(c), the fluctuating pressure coefficients on the back face of the building in case E are very small since the flow field is blocked by the two side parts of the U-shaped model, which in turn leads to the vortex energy and the corresponding wind pressures on the back face being small.

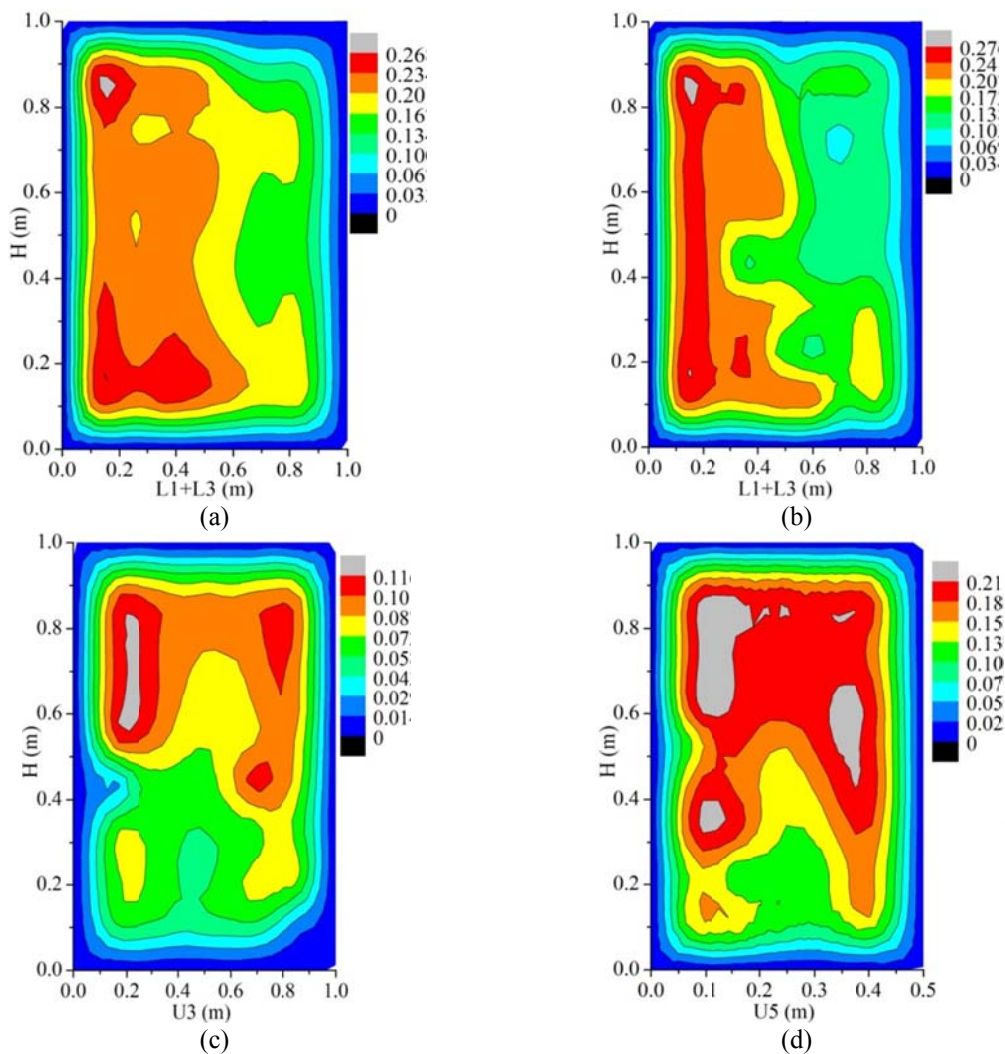


Fig. 14 Fluctuating pressure coefficient contours by numerical simulation: (a) case C and side face, (b) case D and side face, (c) case E and back face and (d) case F and front face

5.3 Vertical and lateral velocity profiles

As more and more high-rise buildings are built in cities, wind flows around these buildings may cause discomfort for pedestrians and damage to structural members and surrounding areas. Although a considerable amount of research on the velocity profiles at various positions around high-rise buildings have been conducted (Kyung *et al.* 2003), detailed studies on the velocity profiles are still necessary for effective structural and wind environment design. Hence, the LES results can be utilized to investigate the velocity profiles around high-rise building models.

To systematically investigate the vertical velocity profiles and flow fields around irregularly shaped bluff bodies, four vertical planes, Plane A to Plane D, sectioned across the building model for Case C and Case E are formulated to show the wind velocity patterns from the numerical simulations. The locations of the planes are shown in Fig. 15. The vertical velocity profiles of the Planes A/B/C/D are presented in Figs. 16 and 17, and the velocity vector fields of Plane A and Plane D are shown in Fig. 18. In the inflow zones ($x/H < -0.25$, see Fig. 19), negligible discrepancies among vertical velocity profiles at different measurement planes are found, and the wind velocity profiles in the inflow zone are well fitted to the log-law profile presented in Section 3. Noticeable discrepancies, however, appear in the different planes in areas, where $-0.25 < x/H < 0$. In the roof zones, the vertical profiles at the position $x/H = 0$ are noticeably different from the profiles at other positions because there is no vortex generation, as shown in Fig. 18, around the position $x/H = 0$ on the roof. In the roof zones where $x/H > 0$, vortices are created after the flow separation, inducing a change in the vertical profiles. The vertical profiles show a C type trend in areas where $1 < z/H < 1.4$. In detail, there is a negative growth of the wind velocity in the region $1 < z/H < 1.15$ and an increasing trend in the region $1.4 < z/H < 1.15$. In the region $z/H > 1.4$, the vertical profiles return to the log-law profile as the influence of the bluff body decreases. As a result, the maximum disturbance scope (MDS), which is defined as the maximum disturbed scope of the flow around building models, induced by blocking effects, is suggested to be mainly in areas $1 < z/H < 1.4$ for the roof zones and $-0.25 < x/H < 0$ for the inflow zones (see Fig. 19).

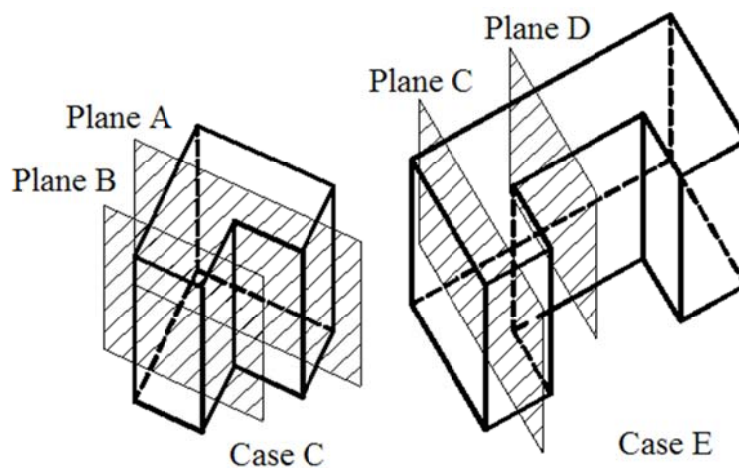


Fig. 15 Selected planes

In wake zones $0 < x/H < 3$, $0 < z/H < 1.1$, the vertical profiles are greatly disturbed by the blocking effect of the bluff bodies and are almost constant vertically, as shown in Figs. 16 and 17. However, in areas $0 < x/H < 3$ and $1.1 < z/H < 1.5$, the wind velocity increases with decrease of the blocking effect. In wake zones $0 < x/H < 3$, $z/H > 1.5$ and $x/H > 3$, $z/H > 0$, the blocking effect gradually decreases to a negligible level, which leads the wind profiles to gradually return to the log-law profiles. Hence, the MDS in the wake zone is mainly found in the region $0 < x/H < 3$, $0 < z/H < 1.5$. In addition, it is worth mentioning that the MDS for case F in the wake zone extends to the region $0 < z/H < 1.7$, which is higher than the wake zones found in other cases. The reason for such an observation is that most of the inflow does not separate from the side zones but from the roof zones, which expands the MDS in the roof and wake zones.

Three measurement planes C1, C2 and C3 in the Y-Z directions, perpendicular to the inflow, were utilized to investigate the lateral velocity profiles and are shown in Fig. 19. The lateral velocity profiles for Cases A/B/C/E at different heights are shown in Fig. 20, and the lateral velocity profiles of Plan C1 and Plan C3 for Case E and Case F are shown in Fig. 21. In addition, the vector field of the wind velocity at a height of $z = 0.5H$ for Case A and Case F are presented in Fig. 22. In general, the recessed downward extent of the lateral profiles decreases with increase of height away from the ground. As shown in Figs. 20(a) and 20(b), the concave degree of the lateral wind profiles at a height of $z/H = 0.25$ is larger than the profiles at a height of $z/H = 0.75$, and the concave degree of the lateral wind profile at a height of $z/H = 0.75$ is larger than the profile at a height of $z/H = 1.25$. This indicates that the wind flow near a bluff body is greatly disturbed, whereas in areas far away from the bluff body, the disturbance is small. For example, the lateral velocity ratios, v/v_{ref} , where v_{ref} is the reference wind velocity, at a height of $z/H = 0.75$ in Fig. 18(a) are 1.76, 1.73, 1.70, 1.59, 1.45 and 1.34 in the range of $-1 < y/H < 0.5$. Therefore, it can be observed that the MDS is mainly concentrated in regions where $-0.5 < y/H < 0.5$ within the two side zones.

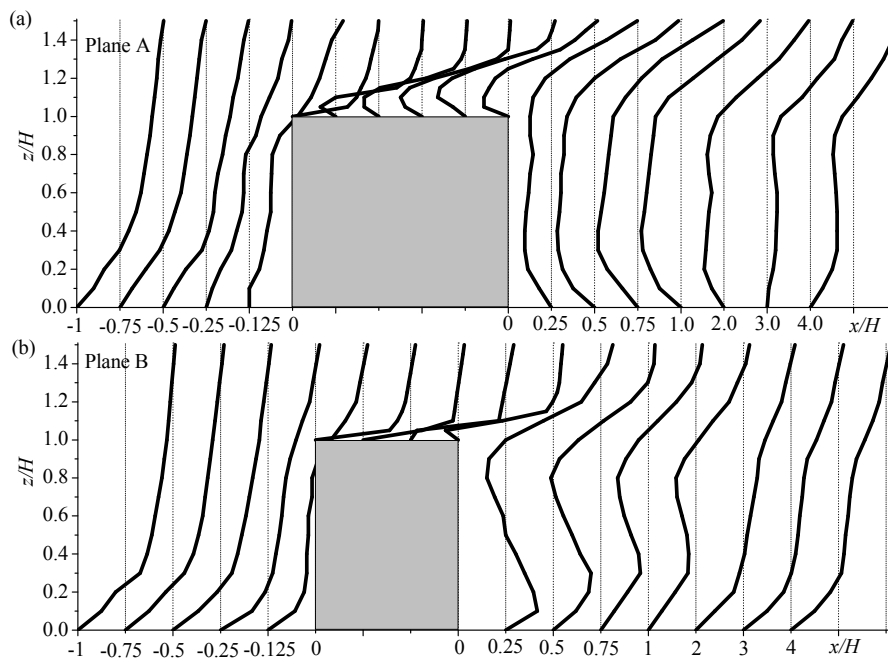


Fig. 16 Vertical velocity profiles of Case C: (a) Plane A and (b) Plane B

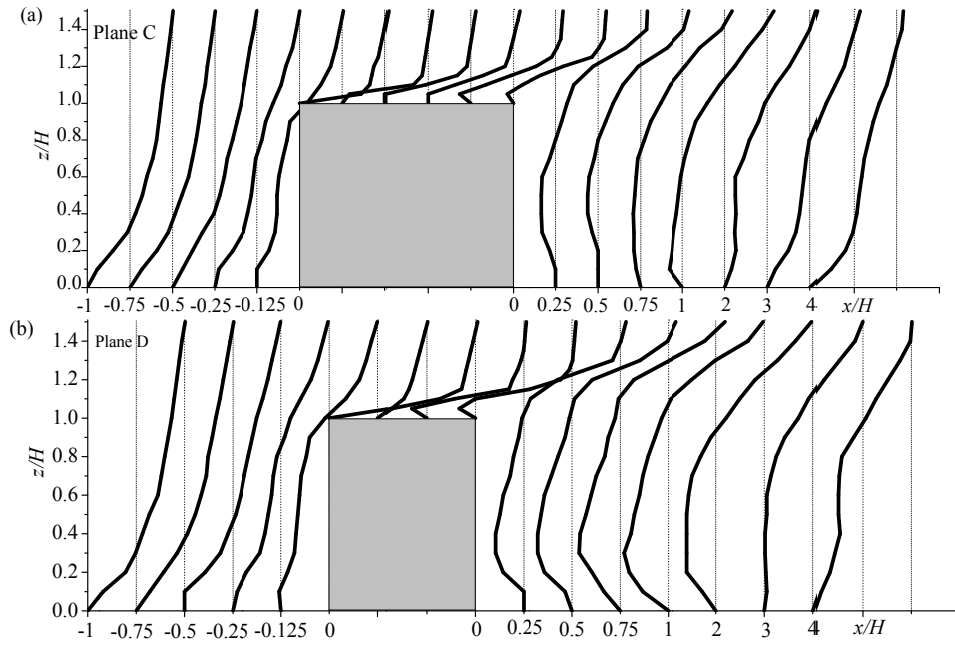


Fig. 17 Vertical velocity profiles of Case E: (a) Plane C and (b) Plane D

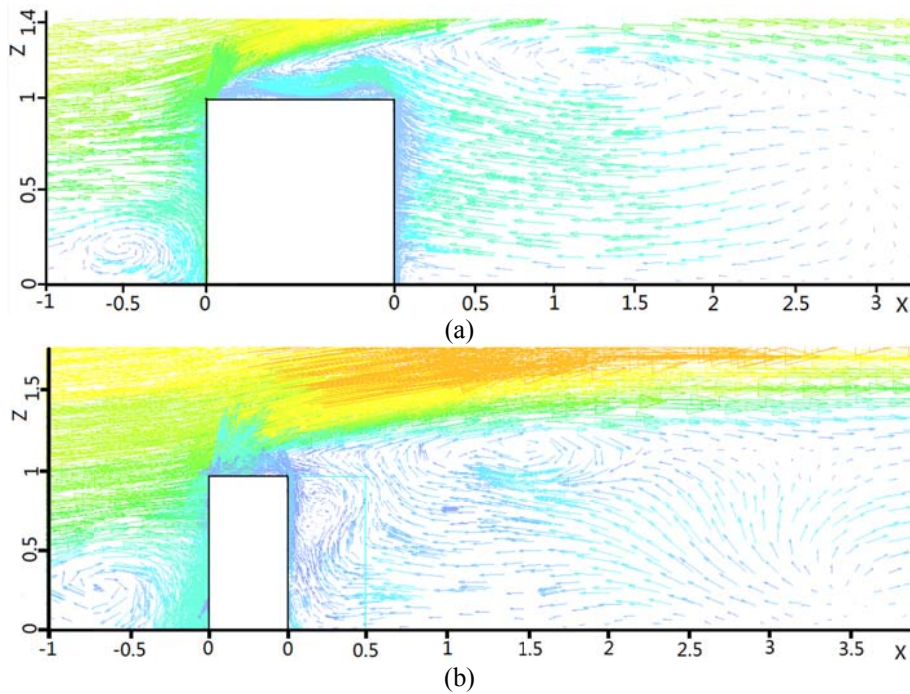


Fig. 18 Velocity vectors of flow field: (a) Case C & Plane A and (b) Case E & Plane D

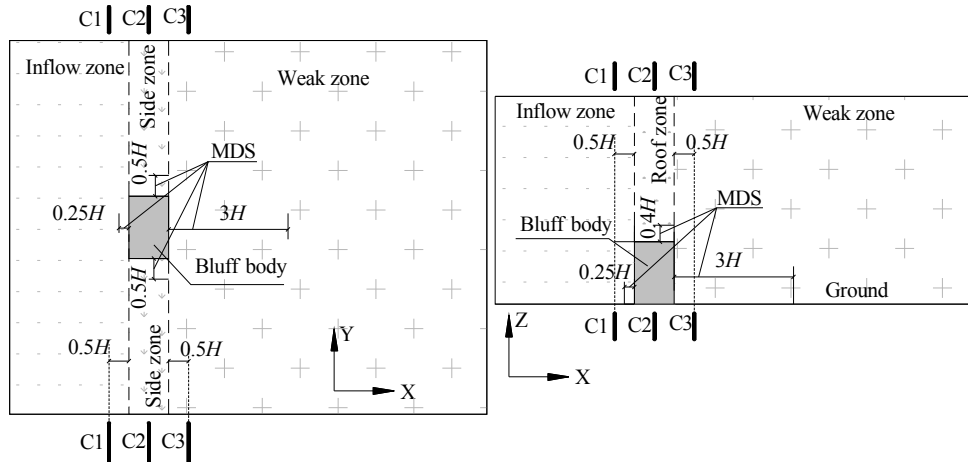


Fig. 19 Model zones and MDS

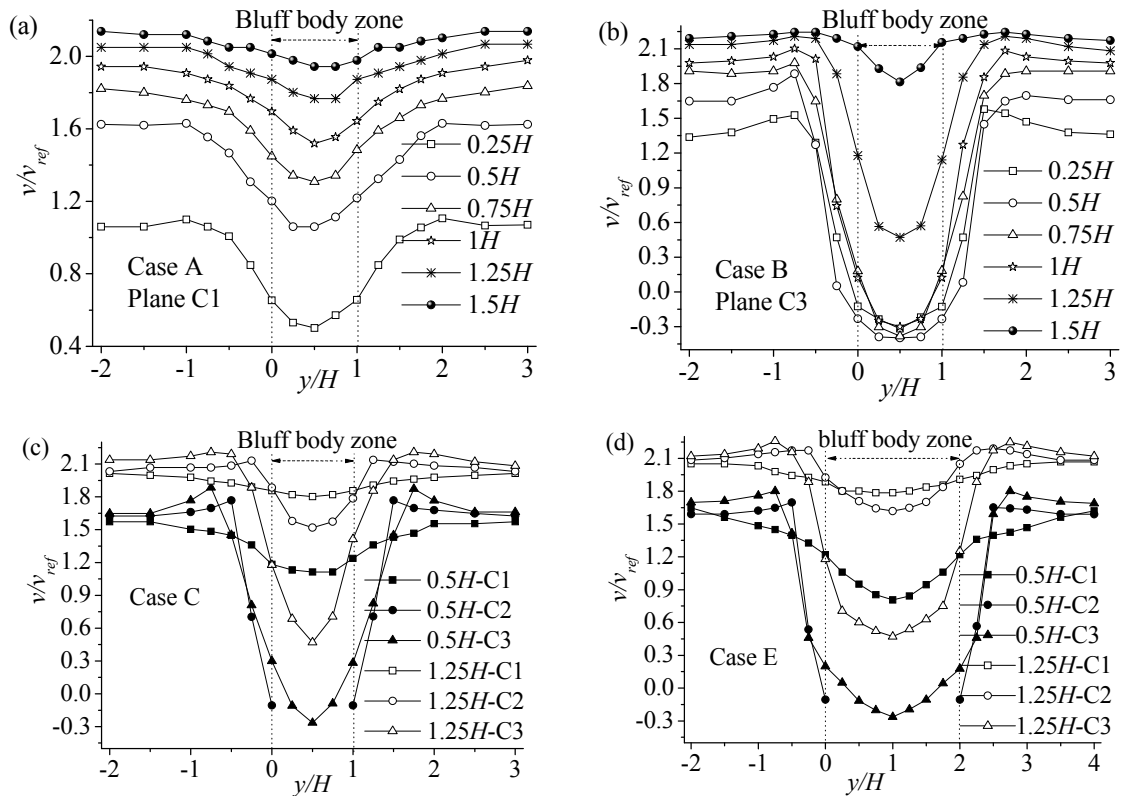


Fig. 20 Lateral velocity profiles: (a) Case A, (b) Case B, (c) Case C and (d) Case E

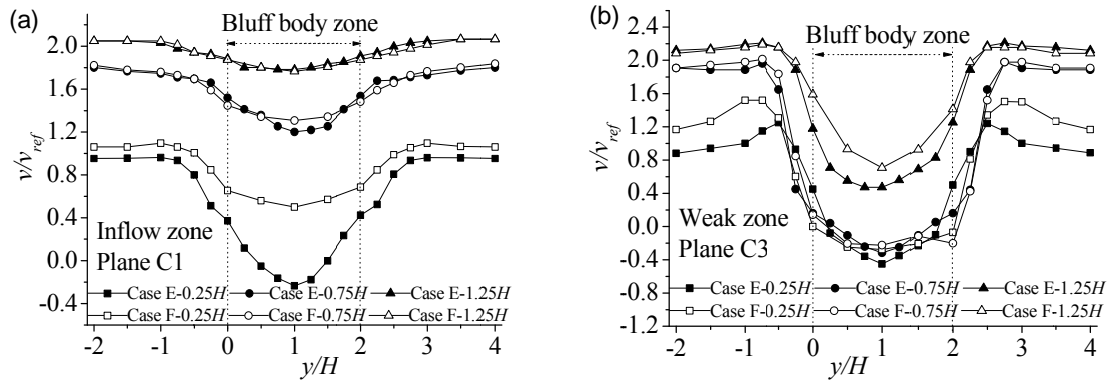


Fig. 21 Lateral velocity profiles: (a) Plane C1 and (b) Plane C3

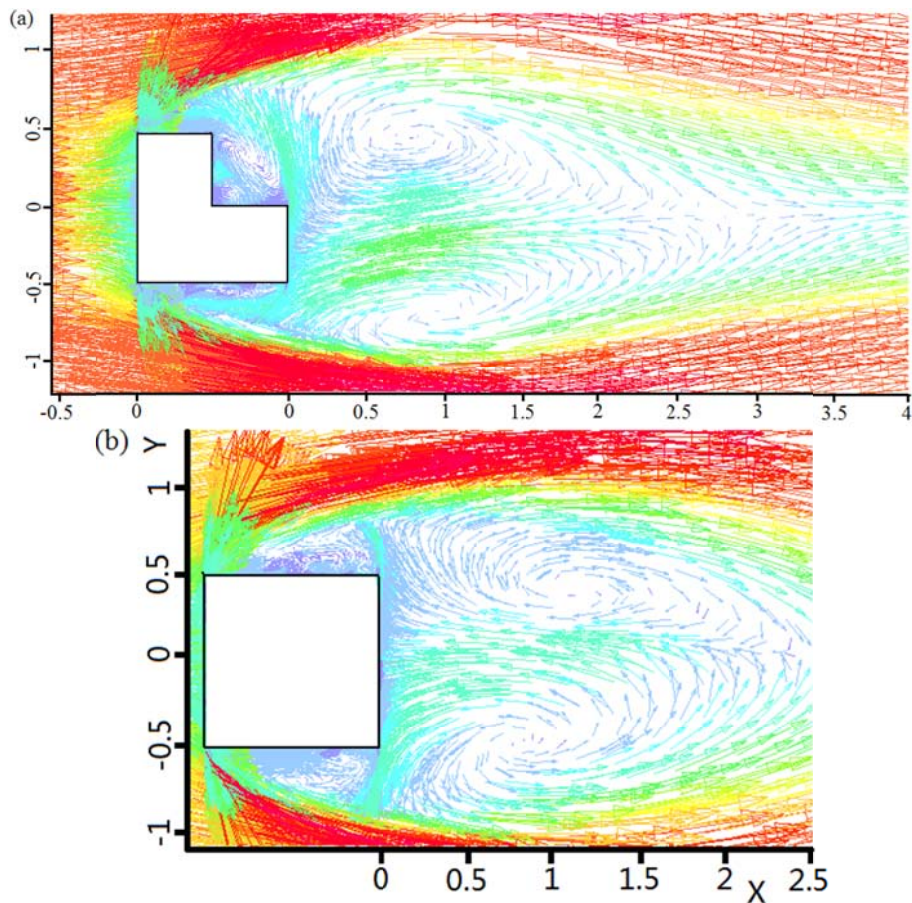


Fig. 22 Lateral vectors of flow field at $z = 0.5H$: (a) Case A and (b) Case F

The lateral wind profiles in the wake zones are most disturbed by the presence of the bluff body, whilst the lateral wind profiles in the inflow zones are barely influenced by the bluff body, as shown in Fig. 22. It can be observed that the disturbance of the lateral profiles caused by the bluff bodies shows almost the same pattern as in the vertical profiles among the inflow, roof and wake zones. Deficiencies among the lateral wind profiles for all six cases decrease gradually with increase of height in the inflow, roof and wake zones, and the trend is more obvious for the profiles in the inflow and roof zones.

6. Conclusions

A Combination Random Flow Generation (CRFG) method for generating the turbulent fluctuating wind velocity time series was developed in this study, which ensured that the generated turbulent fluctuating velocity field satisfies the required statistical characteristics, such as the power spectrum intensity, the spatial correlation coefficient and the turbulent kinetic energy profile. The validity and the feasibility of the CRFG technique to generate the inlet boundary conditions for use in a LES of the wind flow around bluff bodies were verified by comparative analysis among the results obtained by CRFG/RFG simulation and from existing experimental/numerical data.

The CRFG method was then programmed to generate the inlet boundary condition for a LES of the wind field around four irregularly shaped bluff bodied buildings. The pressure coefficients on the building surfaces, calculated based on both wind tunnel test results and numerical simulation. The results were in good agreement, which substantiating the reliability of the LES in terms of simulating both the mean and fluctuating pressures acting on the bluff bodies induced by wind-structure interaction when the inflow boundary condition is generated using the CRFG technique.

The mean pressure coefficients show a consistent distribution on the front faces across different building models. Generally, in the vertical direction, pressures on the front faces decrease initially in the height range $0H \sim 0.25H$, then increase in the range $0.25H \sim 0.8H$ and finally decrease again in the range $0.8H \sim 1.0H$. The lateral variation of the pressures shows a gradual decreasing trend from the centerline to both sides. The maximum and minimum pressures are located at heights of approximately $0.8H$ and $0.25H$ from the ground, respectively. The fluctuating pressure coefficients are significantly influenced by the vortex behavior, with strong vortex motions with high energy generating fluctuating pressures with large amplitudes. The distribution of the negative mean pressure coefficient provides a feasible way to predict the magnitude of fluctuating pressure coefficients because the negative mean pressure coefficient and the fluctuating pressure coefficient show a similar variation.

The velocity profiles in the wake zones are greatly disturbed by the presence of the bluff body, while the profiles in the inflow zones are less affected. The disturbed intensity shows a gradual decreasing trend with increase of the distance away from the bluff body. In general, the maximum disturbance scopes are located at $0.25H$ in inflow zones, $0.4H$ in the roof zones, $0.5H$ in the both side zones and $3H$ in the weak zones, where H is the height of the bluff body.

Acknowledgements

The study reported in this paper is carried out under the support of the RGC Direct Allocation Grants (Project No. DAG11EG06), National Natural Science Foundation of China (No. 51408140), Doctoral Foundation of China Education Ministry (No. 20134410120003) and Technology Foundation of Guangzhou City (No. 2014J4100122), to which the authors would like to express the gratitude.

References

- ADINA R&D, Inc. (2005), *Theory and Modeling Guide, Volume I, II and III*, Watertown, USA, <http://www.adina.com>.
- Barić, E., Džijan, I. and Kozmar, H. (2010), "Numerical simulation of wind characteristics in the wake of a rectangular building submitted to realistic boundary layer conditions", *Transactions of Famena*, **34**(3), 1-10.
- Batten, P., Goldberg, U. and Chakravarthy, S. (2004), "Interfacing statistical turbulence closures with large-eddy simulation", *AIAA J.*, **42**(3), 485-492.
- Bazdidi-Tehrani, F., Ghafouri, A. and Jadidi, M. (2013), "Grid resolution assessment in large eddy simulation of dispersion around an isolated cubic building", *J. Wind Eng. Ind. Aerod.*, **121**, 1-15.
- Blocken, B., Carmeliet, J. and Stathopoulos, T. (2007), "CFD evaluation of wind speed conditions in passages between parallel buildings-effect of wall-function roughness modifications for the atmospheric boundary layer flow", *J. Wind Eng. Ind. Aerod.*, **95**(9-11), 941-962.
- Blocken, B., Stathopoulos, T. and Carmeliet, J. (2007), "CFD simulation of the atmospheric boundary layer: wall function problems", *Atmos Environ.*, **41**(2), 238-252.
- Camarri, S., Salvetti, M.V., Koobus, B. and Dervieux, A. (2002), "Large-eddy simulation of a bluff-body flow on unstructured grids", *Int. J. Numer Meth. Fl.*, **40**(11), 1431-1460.
- Celik, I., Cehreli, Z.N. and Yavuz, I. (2005), "Index of resolution quality for large eddy simulation", *J. Fluids Eng.*, **127**(5), 949-958.
- China Ministry of Construction (2012), *Loading code for the design of building structures*, GB 50009-2012, China Building Industry Press, Beijing.
- Churchfield, M.J., Lee, S., Michalakes, J. and Moriarty, P.J. (2012), "A numerical study of the effects of atmospheric and wake turbulence on wind turbine dynamics", *J. Turbul.*, **13**, N14.
- Dagnew, A.K. and Bitsuamlak, G.T. (2014), "Computational evaluation of wind loads on a standard tall building using LES", *Wind Struct.*, **18**(5), 567-598.
- Franke, J., Hellsten, A., Schlünzen, H. and Carissimo, B. (2007), *Best practice guideline for the CFD simulation of flows in the urban environment*, COST Action 732.
- Gorlé, C., Beeck, J. and Van, R.P. (2010), "Dispersion in the wake of a rectangular building: validation of two reynolds-averaged navier-stokes modelling approaches", *Bound. -Lay. Meteorol.*, **137**(1), 115-133.
- Gomes, M.G., Moret, R.A. and Pedro M. (2005), "Experimental and numerical study of wind pressures on irregular-plan shapes", *J. Wind Eng. Ind. Aerod.*, **93**, 741-756.
- Gousseau, P., Blocken, B. and Van H.G.J.F. (2013), "Quality assessment of Large-Eddy Simulation of wind flow around a high-rise building: Validation and solution verification", *Comput. Fluids*, **79**, 120-133.
- Hoshiya, M. (1972), "Simulation of multi-correlated random processes and application to structural vibration problems", *Proceedings of JSCE*, **204**, 121-128.
- Huang, S.H., Li, Q.S. and Wu, J.R. (2010), "A general inflow turbulence generator for large eddy simulation", *J. Wind Eng. Ind. Aerod.*, **98**, 600-617.
- Huang, S.H., Li, Q.S. and Xu, S.L. (2006), "Numerical evaluation of wind effects on a tall steel building by CFD", *J. Constr. Steel Res.*, **63**(5), 1-16.
- Hinze, J.O. (1975), *Turbulence*, McGraw-Hill, New York.

- Jones, W.P. and Launder, B.E. (1972), "The prediction of laminarization with a 2-equation model of turbulence", *In. J. Heat Mass Tran.*, **15**, 301-318.
- Keating, A., Piomelli, U., Balaras, E. and Kaltenbach, H.J. (2004), "A priori and a posteriori tests of inflow conditions for large-eddy simulation", *Phys. Fluids*, **16**, 4696.
- Kim, K.C., Ji, H.S. and Seong, S.H. (2003), "Flow structure around a 3-D rectangular prism in a turbulent boundary layer", *J. Wind Eng. Ind. Aerod.*, **91**, 653-669.
- Klein, M., Sadiki, A. and Janicka, J. (2003), "A digital filter based generation of inflow data for spatially developing direct numerical or large eddy simulations", *J. Comput. Phys.*, **186**, 652-665.
- Kondo, K., Murakami, S. and Mochida, A. (1997), "Generation of velocity fluctuations for inflow boundary condition of LES", *J. Wind Eng. Ind. Aerod.*, **67-68**, 51-64.
- Kozmar, H. (2011), "Wind-tunnel simulations of the suburban ABL and comparison with international standards", *Wind Struct.*, **14**(1), 15-34.
- Kraichnan, R.H. (1970), "Diffusion by a random velocity field", *Phys. Fluids*, **13**(1), 22-31.
- Labovský, J. and Jelemenský, L. (2011), "Verification of CFD pollution dispersion modelling based on experimental data", *J. Loss Prevent. Proc.*, **24** (2), 166-177.
- Li, Q.S., Xiao, Y.Q., Wong, C.K. and Jeary, A.P. (2004), "Field measurements of typhoon effects on a super tall building", *Eng. Struct.*, **26**(2), 233-244.
- Li, Q.S., Xiao, Y.Q. and Wong, C.K. (2005), "Full-scale monitoring of typhoon effects on super tall buildings", *J. Fluids Struct.*, **20**(5), 697-717.
- Li, Q.S., Xiao, Y.Q., Fu, J.Y. and Li, Z.N. (2007), "Full scale measurements of wind effects on the Jin Mao Building", *J. Wind Eng. Ind. Aerod.*, **95**(6), 445-466.
- Lumley, J.L. and Panofsky, H.A. (1964), *The Structure of Atmospheric Turbulence*, Wiley- Interscience, New York, 239.
- Mathey, F., Cokljat, D., Bertoglio, J.P. and Sergent, E. (2006), "Assessment of the vortex method for large eddy simulation inlet conditions", *Prog. Comput. Fluid Dy.*, **6**(1-3), 58-67.
- Murakami, S. (1998), "Overview of turbulence models applied in CWE-1997", *J. Wind Eng. Ind. Aerod.*, **76**, 1-24.
- Meng, Y. and Hibi, K. (1998), "Turbulent measurements of the flow field around a high-rise building", *J. Wind Eng.*, **76**, 55-64.
- Murakami, S. (1993), "Comparison of various turbulence models applied to a bluff body", *J. Wind Eng. Ind. Aerod.*, **46-47**, 21-36.
- O'Sullivan, J.P., Archer, R.A. and Flay, R.G.J. (2011), "Consistent boundary conditions for flows within the atmospheric boundary layer", *J. Wind Eng. Ind. Aerod.*, **99**, 65-77.
- Parente, A., Gorié, C. and Beeck, J. (2011), "A comprehensive modelling approach for the neutral atmospheric boundary layer: consistent inflow conditions, wall function and turbulence model", *Bound. – Lay. Meteorol.*, **140**, 411-428.
- Richard, J.S., Jason, G. and Charles, M. (2014), "A concurrent precursor inflow method for large eddy simulation and applications to finite length wind farms", *Renew. Energ.*, **68**, 46-50.
- Schluter, J.U., Pitsch, H. and Moin, P. (2004), "Large eddy simulation inflow conditions for coupling with Reynolds-averaged flow solvers", *AIAA J.*, **42**(3), 478-484.
- Sepe, V. and Vasta, M. (2014), "Wind-tunnel tests on high-rise buildings: wind modes and structural response", *Wind Struct.*, **18**(1), 37-56.
- Sergent, E. (2002), *Vers une méthode de couplage entre la simulation des grandes échelles et les modèles statistiques*, PhD thesis, Ecole doctorale MEGA, Ecole Centrale de Lyon.
- Simiu, E. and Scanlan, R.H. (1996), *Wind effects on structures*, 3rd Ed., Wiley, New York.
- Smirnov, A., Shi, S. and Celik, I. (2001), "Random flow generation technique for large-eddy simulations and particle-dynamics modeling", *ASME J. Fluids Eng.*, **123**, 359-371.
- Tamura, T. (2000), "Towards practical use of LES in wind engineering", *J. Wind Eng. Ind. Aerod.*, **96**(10-11), 1451-1471.
- Tse, K.T., Wang, D.Y. and Zhou, Y. (2013), "Wind pressure characteristics for a double tower high-rise structure in a group of buildings", *Wind Struct.*, **16**(5), 491-515.

- Tse, K.T., Yang, Y., Shum, K.M and Xie, Z.N. (2013), "Numerical simulation of wind loads on noise mitigation structures along roadsides", *Wind Struct.*, **17**(3), 299-315.
- Tunay, T., Sahin, B. and Akilli, H. (2013), "Experimental and numerical studies of the flow around the Ahmed body", *Wind Struct.*, **17**(5), 515-535.
- Tominaga, Y., Mochida, A., Yoshie, R., Kataoka, H., Nozu, T. and Yoshikawa, M. (2008), "AIJ guidelines for practical applications of CFD to pedestrian wind environment around buildings", *J. Wind Eng. Ind. Aerod.*, **96**, 1749-1761.
- Wang, D.Y. and Zhou, Y. (2010), "Numerical study on spatial wind-pressure distribution characteristic of three-dimensional U-shaped body", *J. Wuhan Univ. Technol.*, **9**, 157-160. (In Chinese)
- Wienken, W., Stiller, J. and Keller, A. (2006), "A method to predict cavitation inception using large-eddy simulation and its application to the flow past a square cylinder", *J. Fluids Eng.*, **128**(2), 316-326.
- Yang, W., Quan, Y., Jin, X.Y., Tamura, Y. and Gu, M. (2008), "Influences of equilibrium atmosphere boundary layer and turbulence parameter on wind loads of low-rise building", *J. Wind Eng. Ind. Aerod.*, **96**, 2080-2092.
- Yang, Y., Gu, M., Chen, S.Q. and Jin, X.Y. (2009), "New inflow boundary conditions for modeling the neutral equilibrium atmospheric boundary layers in Computational Wind Engineering", *J. Wind Eng. Ind. Aerod.*, **97**(2), 88-95.
- Yang, Y., Jin, X.Y., Tse, K.T. and Gu, M. (2012), "Verification of a tree canopy model and its application in wind environment optimization design of high-rise buildings", *Wind Struct.*, **15**(5), 409-421.

